Available online at www.sciencedirect.com
SCIENCE DIRECT®
Journal of Solid State Chemistry 177 (2004) 1704–1712
JOURNAL OF SOLID STATE CHEMISTRY
http://elsevier.com/locate/jssc

Conduction band splitting and transport properties of Bi_2Se_3

J. Navrátil,[a,*] J. Horák,[a] T. Plecháček,[a] S. Kamba,[b] P. Lošťák,[c] J.S. Dyck,[d] W. Chen,[d] and C. Uher[d]

[a] *Joint Laboratory of Solid State Chemistry, Academy of Sciences of the Czech Republic, University of Pardubice, Studentská 84, Pardubice 530 03, Czech Republic*

[b] *Institute of Physics, Academy of Sciences of the Czech Republic, Na Slovance 2, CZ-182 21 Praha 8, Czech Republic*

[c] *Department of General and Inorganic Chemistry, Faculty of Chemical Technology, University of Pardubice, Čs. Legií 565, Pardubice 532 10, Czech Republic*

[d] *Department of Physics, University of Michigan, Ann Arbor, MI 48109-1120, USA*

Received 8 September 2003; received in revised form 18 December 2003; accepted 30 December 2003

Abstract

Detailed transport studies of single crystals of Bi_2Se_3 were made in the temperature range of 2–300 K, and the data were analyzed in terms of a model consisting of two groups of electrons—a centrosymmetrical lower conduction band and an upper conduction band located away from the Γ-point. Very good agreement with the experimental data is obtained assuming the electrons are scattered on acoustic phonons and ionized impurities. A rather strong influence of the latter mechanism is attributed to a large number of charged selenium vacancies in Bi_2Se_3. The fitted transport parameters were used to calculate the electronic portion of the thermal conductivity that, in turn, allowed for the determination of the lattice thermal conductivity. The Debye model provides a good approximation to the temperature dependence of the lattice thermal conductivity.
© 2004 Elsevier Inc. All rights reserved.

Keywords: Transport properties; Bi_2Se_3; Two-band model; Carrier scattering

1. Introduction

Bi_2Se_3 belongs to a class of narrow-gap layered semiconductors with the tetradymite structure (space group $R\bar{3}m$-D^5_{3d}). Solid solutions of the family (Bi_2Se_3, Bi_2Te_3, and Sb_2Te_3) are important for thermoelectric applications [1,2] due to their high thermoelectric figure of merit at ambient temperatures. The physical properties establishing Bi_2Se_3 as a semiconductor were studied earlier [3–6]. The underlying band structure [7–9] and the nature of the charge carrier scattering mechanisms were also determined previously [10–12]. The principal minimum of the conduction band in Bi_2Se_3 is located at the center of the Brillouin zone (Γ-point) and is represented by a single ellipsoid. One calculation [7] indicates the existence of a second conduction band minimum located away from the Γ-point and lying about 80 meV above the minimum of the principal conduction band. In more recent calculations [8,9], this upper conduction band (UCB) is more than 250 meV higher than the lower conduction band (LCB). It should be mentioned, however, that the effect of Se vacancies was not taken into consideration in any of the band structure calculations.

To contribute to the understanding of the discrepancies in the theoretical calculations, we tried to interpret our data according to new experimental findings—the existence of the two conduction bands in band structure of Bi_2Se_3. A possibility of the existence of a second conduction band was suggested in the Shubnikov–de Haas experiments of Koehler [11] on Bi_2Se_3 doped to high electron carrier density ($\sim 10^{18}\,cm^{-3}$), though the authors remarked that the speculation was somewhat inconclusive because data could not be extended to magnetic fields greater than 15 T. Recently, results of cyclotron resonance to much higher magnetic fields became available [13], which indicated the presence of a second or UCB with electrons of smaller effective mass at an energy of approximately 40 meV above the Γ-point or LCB. However, the exact location within the Brillouin zone was not addressed. The existence of two

*Corresponding author. Fax: +420-466036011.
E-mail address: jiri.navratil@upce.cz (J. Navrátil).

0022-4596/$ - see front matter © 2004 Elsevier Inc. All rights reserved.
doi:10.1016/j.jssc.2003.12.031

conduction bands not too widely spaced in energy implies the presence of two groups of carriers with potentially different effective masses in n-type Bi_2Se_3 crystals.

In the light of these new results concerning the conduction band edges in Bi_2Se_3 we have tried to elaborate our previous single-valley conduction band model published in this journal [14] and to assess the influence of the two groups of electrons on the transport properties over a wide temperature range. Using a mixed scattering model [15] we have attempted to estimate contributions of the individual scattering mechanisms that govern the transport parameters. The results of the model were further used to calculate the electronic part of the thermal conductivity and, in turn, to determine the contribution due to lattice phonons. Our analysis suggests that the UCB has a multi-valley character and thus is located away from the center of symmetry.

2. Experimental details

Single crystals of Bi_2Se_3 were grown by the Bridgman method. The starting polycrystalline substance was synthesized from Bi and Se elements of 5 N purity in evacuated conical silica ampoules at 1050 K for 48 h. The growth of the crystal was carried out in the same ampoule with a pulling rate of 1.3 mm h^{-1}. Rectangular samples with dimensions of $2.5 \times 3 \times 10\,mm^3$ were cut from the ingot using a spark-erosion technique. Infrared reflectivity measurements $R_{\perp c}$ were performed with an infrared Fourier spectrometer Bruker IFS 113v equipped with room temperature DTGS pyroelectric detectors on fresh, natural (0001) cleavage surfaces with polarization $\mathbf{E} \perp c$. $\mathbf{E}$ is the electrical field of the radiation and c is the trigonal, optical axis. Spectra were obtained in the range 400–3000 cm^{-1} with a resolution of 2 cm^{-1}. A continuous flow Oxford CF 104 cryostat with KBr windows was used for low-temperature optical measurements down to 10 K. Temperatures above 80 K were stabilized with an accuracy of ± 0.5 K, while at low temperatures the accuracy of ± 2 K was achieved.

Transport properties were measured over the temperature range of 2–300 K. Galvanomagnetic studies were made in a cryostat equipped with a 5.5 T superconducting magnet and with the aid of a Linear Research ac bridge with 16 Hz excitation. Thermal transport measurements were carried out in an adiabatic cryostat with two radiation shields. Thermal gradients were measured using a combination of Ge thermometers (2–25 K) and copper–constantan thermocouples (20–300 K). For the Nernst–Ettingshausen experiments, Cernox thermometers were used due to their small magnetoresistance. Seebeck voltages were measured with the copper legs of the thermocouples and the sample thermopower was corrected for the contribution from the copper wires. Thermal conductivity measurements were corrected for a radiation loss by suspending the sample by its connecting wires and determining the power needed to supply to the sample heater in order to achieve the same average sample temperature as used in the actual experiment. Radiation losses at 300 K amounted to a 10% correction and became negligible below 150 K. All measurements are done in a configuration where the current and thermal gradients are applied along the binary axis, the magnetic field is parallel to the trigonal axis c, and the Hall (or Nernst) field is measured along the bisectrix axis, i.e., all measurements including reflectivity were performed along natural (0001) planes (perpendicular to the c-axis).

3. Model

3.1. Determination of the reduced Fermi level and the concentration of both types of electrons

If two bands contribute to the free carrier transport, the real (ε_1) and imaginary part (ε_2) of the dielectric constant can be written as, e.g. [16],

$$\begin{aligned}\varepsilon_1 &= n^2 - k^2 \\ &= \varepsilon_{\infty\perp c}\left[1 - \left(\frac{n_1 e^2}{m^*_{1\perp c}\,\varepsilon_0\,\varepsilon_{\infty\perp c}}\frac{1}{\omega^2 + 1/\tau_1^2}\right.\right. \\ &\quad \left.\left. + \frac{n_2 e^2}{m^*_{2\perp c}\,\varepsilon_0\,\varepsilon_{\infty\perp c}}\frac{1}{\omega^2 + 1/\tau_2^2}\right)\right], \qquad (1)\end{aligned}$$

$$\begin{aligned}\varepsilon_2 &= 2nk \\ &= \varepsilon_{\infty\perp c}\left(\frac{n_1 e^2}{m^*_{1\perp c}\,\varepsilon_0\,\varepsilon_{\infty\perp c}}\frac{1}{\omega\tau_1}\frac{1}{\omega^2 + 1/\tau_1^2}\right. \\ &\quad \left. + \frac{n_2 e^2}{m^*_{2\perp c}\,\varepsilon_0\,\varepsilon_{\infty\perp c}}\frac{1}{\omega\tau_2}\frac{1}{\omega^2 + 1/\tau_2^2}\right), \qquad (2)\end{aligned}$$

where $\varepsilon_{\infty\perp}$ is the high-frequency dielectric constant, ε_0 is vacuum permittivity, e is electron charge, $m^*_{i\perp c}$ ($i = 1, 2$) are effective masses, n_i are concentrations of the individual carriers and τ_i are their optical relaxation times. Indices $i = 1$ and 2 are used to designate electrons located in the lower (LCB) and upper (UCB) conduction bands, respectively.

In a region where $\omega^2 \gg 1/\tau_1^2$ and $\omega^2 \gg 1/\tau_2^2$, the above equations simplify to

$$\varepsilon_1 = \varepsilon_{\infty\perp c} - \frac{e^2}{\varepsilon_0\omega^2}\left(\frac{n_1}{m^*_{1\perp c}} + \frac{n_2}{m^*_{2\perp c}}\right) \qquad (3)$$

and

$$\varepsilon_2 = \frac{e^2}{\omega^3}\left(\frac{n_1}{m^*_{1\perp c}\tau_1} + \frac{n_2}{m^*_{2\perp c}\tau_2}\right). \qquad (4)$$

One can see immediately that under the above conditions the functional form of ε_1 and ε_2 is similar regardless of whether one considers a single or a two-band model. Moreover, the value of $n/m^*_{\perp c}$ obtained by fitting the reflectance spectra according to a single band model can be expressed as

$$\frac{n}{m^*_{\perp c}} = \frac{n_1}{m^*_{1\perp c}} + \frac{n_2}{m^*_{2\perp c}}. \tag{5}$$

Using Fermi–Dirac statistics, concentrations of both types of electrons are given by

$$n_1 = 4\pi\left(\frac{2m^*_{1d}k_{\mathrm{B}}T}{h^2}\right)^{3/2} F_{1/2}(\eta^*) \tag{6}$$

and

$$n_2 = 4\pi\left(\frac{2m^*_{2d}k_{\mathrm{B}}T}{h^2}\right)^{3/2} F_{1/2}(\eta^* - \Delta^*), \tag{7}$$

where m^*_{id} are density of states effective masses, k_{B} is the Boltzmann constant, T is temperature, h is the Planck constant, $\eta^* = \eta/k_{\mathrm{B}}T$ is the reduced chemical potential of an electron (reduced Fermi energy), $\Delta^* = \Delta/k_{\mathrm{B}}T$ ($\Delta = 40$ meV according to Ref. [13]) is the reduced energy splitting of the lower and higher conduction bands. $F_{1/2}(\eta^*)$ and $F_{1/2}(\eta^* - \Delta^*)$ are Fermi integrals of the type

$$F_n(\eta^*) = \int_0^\infty \frac{x^n}{1 + \mathrm{e}^{x-\eta^*}}\,\mathrm{d}x. \tag{8}$$

3.2. Galvanomagnetic transport properties

To determine mobilities of both types of electrons one can use relations for the conductivity, Hall coefficient, and magnetoresistance.

The total electrical conductivity is expressed as

$$\sigma_{\perp c} = \sum_i \sigma_i = \sum_i e n_i \mu_i = \sum_i \frac{e^2 n_i \langle \tau_i \rangle}{m^*_{i\perp c}}, \tag{9}$$

where the summation is over two types of electrons. Here μ_i are the respective drift mobilities of the carriers and $\langle \tau_i \rangle$ are their relaxation times. As we discuss in more detail later, we use a mixed scattering model comprising acoustic and ionized impurity scattering in our analysis of the transport data. A combined influence of the two distinct scattering mechanisms is conveniently handled using the approach of Fistul [15] whereby the overall relaxation time is written as

$$\frac{1}{\tau} = \frac{1}{\tau_{\mathrm{ac}0}x^{*-1/2}} + \frac{1}{\tau_{\mathrm{ii}0}x^{*3/2}}. \tag{10}$$

Here, $\tau_{\mathrm{ac}0}$ and $\tau_{\mathrm{ii}0}$ are energy-independent relaxation times for acoustic scattering and ionized impurity scattering, respectively, and x^* is the average reduced energy of carriers. By introducing $a^2 = \tau_{\mathrm{ac}0}/\tau_{\mathrm{ii}0}$, one can write Eq. (10) as

$$\tau = \frac{\tau_{\mathrm{ac}0}x^{*3/2}}{x^{*2} + a^2}. \tag{11}$$

Using this formalism, the conductivities of both types of carriers are:

$$\sigma_1 = \frac{4\pi e^2}{m^*_{1\perp c}h^3}(2m^*_{1d}k_{\mathrm{B}}T)^{3/2}\frac{2}{3}\tau_{1\mathrm{ac}0}\,\Phi_3(\eta^*, a_1), \tag{12}$$

$$\sigma_2 = \frac{4\pi e^2}{m^*_{2\perp c}h^3}(2m^*_{2d}\,k_{\mathrm{B}}\,T)^{3/2}\frac{2}{3}\tau_{2\mathrm{ac}0}\,\Phi_3(\eta^* - \Delta^*, a_2), \tag{13}$$

where

$$\Phi_n(\eta^*, a) = \int_0^\infty \frac{(x^*)^n \mathrm{e}^{x^*-\eta^*}}{[(x^*)^2 + a^2][1 + \mathrm{e}^{x^*-\eta^*}]^2}\,\mathrm{d}x^*. \tag{14}$$

The Hall coefficient for a two-band model in a weak magnetic field ($\sigma R_H B \ll 1$ where B is the intensity of magnetic field and $R_{H\perp c}$ stands for the Hall coefficient), is given by

$$R_{H\perp c} = \frac{1}{\sigma^2}\sum_i R_{Hi}\sigma_i^2 = \frac{e}{\sigma^2}\sum_i n_i\mu_i^2 A_i\gamma_i, \tag{15}$$

where A_i are Hall factors and γ_i are structural factors. The Hall effect we consider here (R_{123}) is the one where the current density and the transverse electric field are in the basal plane of the crystal, and the magnetic field is applied perpendicular to the basal plane. From the calculated values of η^* and for the considered ratio of the scattering mechanisms we determined Hall factors A_i according to the following equations:

$$A_1 = \frac{3}{2}\frac{F_{1/2}(\eta^*)\Phi_{9/2}(\eta^*, a_1)}{[\Phi_3(\eta^*, a_1)]^2}. \tag{16a}$$

and

$$A_2 = \frac{3}{2}\frac{F_{1/2}(\eta^* - \Delta^*)\Phi_{9/2}(\eta^* - \Delta^*, a_2)}{[\Phi_3(\eta^* - \Delta^*, a_2)]^2} \tag{16b}$$

Weak field magnetoresistance for a semiconductor with two types of carriers is, according to Ref. [17], given as

$$\frac{\Delta\rho}{\rho} = \left\{\frac{(\sigma_1 + \sigma_2)}{(\sigma_1 + \sigma_2)^2 + H^2\sigma_1^2\sigma_2^2(R_{H1} + R_{H2})^2}\right.$$
$$\left.[(\sigma_1 + \sigma_2) + H^2\sigma_1\sigma_2(\sigma_1 R_{H1} + \sigma_2 R_{H2})] - 1\right\}. \tag{17}$$

Considering a relatively high degeneracy of both carriers (and low magnetic field), one can easily derive the weak field magnetoresistance coefficient

$$H_{0\perp c} = \frac{1}{B^2}\frac{\sigma_0 - \sigma_B}{\sigma_B} = \frac{1}{\sigma^2}\sigma_1\sigma_2(\sigma_1 R_{H1} - \sigma_2 R_{H2})^2$$
$$= \frac{e^2}{\sigma^2}n_1 n_2 \mu_1\mu_2(A_1\gamma_1\mu_1 - A_2\gamma_2\mu_2)^2. \tag{18}$$

3.3. Thermal transport parameters

The chosen scattering parameters must also be applicable and govern the behavior of the thermal transport properties such as the Seebeck effect and Nernst–Ettingshausen effect, and the electronic part of the thermal conductivity. Seebeck coefficient for the two-band model is expressed as

$$S_{\perp c} = \frac{S_1\sigma_1 + S_2\sigma_2}{\sigma} = -\frac{k_B}{e}\left[\frac{\Phi_4(\eta^*, a_1)}{\Phi_3(\eta^*, a_1)} - \eta^*\right]\frac{\sigma_1}{\sigma} - \frac{k_B}{e}\left[\frac{\Phi_4(\eta^* - \Delta^*, a_2)}{\Phi_3(\eta^* - \Delta^*, a_2)} - (\eta^* - \Delta^*)\right]\frac{\sigma_2}{\sigma}. \quad (19)$$

A low magnetic field formula for the Nernst–Ettingshausen coefficient, when two types of electrons are participating in the transport, is given by [17]

$$Q_{\perp c} = \frac{Q_1\sigma_1\sigma + Q_2\sigma_2\sigma + \sigma_1\sigma_2(R_{H_1}\sigma_1 - R_{H_2}\sigma_2)(S_1 - S_2)}{\sigma^2}. \quad (20)$$

Here Q_i $(i = 1, 2)$ stands for the individual Nernst–Ettingshausen coefficients of the two kinds of electrons,

$$Q_1 = \frac{k_B}{m_0 m^*_{1d}}\tau_{1ac0} \times \frac{\Phi_{9/2}(\eta^*, a_1)\Phi_4(\eta^*, a_1) - \Phi_{11/2}(\eta^*, a_1)\Phi_3(\eta^*, a_1)}{[\Phi_3(\eta^*, a_1)]^2}. \quad (21)$$

For the second band ($i = 2$), the integrals $\Phi_n(\eta^*, a_1)$ are replaced with $\Phi_n(\eta^* - \Delta^*, a_2)$ to reflect the character of the UCB. Finally, the electronic part of the thermal conductivity can be written as

$$\kappa_{e\perp c} = \kappa_{e1\perp c} + \kappa_{e2\perp c} = \sigma_1 L_1 T + \sigma_2 L_2 T, \quad (22)$$

where L_1 and L_2 are the Lorenz numbers of the two carriers, which have the form

$$L_1 = \frac{k_B^2}{e^2}\frac{\Phi_3(\eta^*, a_1)\Phi_5(\eta^*, a_1) - [\Phi_4(\eta^*, a_1)]^2}{[\Phi_3(\eta^*, a_1)]^2}. \quad (23)$$

The relation for L_2 differs from L_1 only in that the integrals $\Phi_n(\eta^*, a_1)$ are replaced with $\Phi_n(\eta^* - \Delta^*, a_2)$.

4. Results

The following parameters according to Ref. [13] were used as input data in the analysis: $m^*_{1\perp c} = 0.105m_0$, $m^*_{2\perp c} = 0.075m_0$, $m^*_{1d} = 0.123m_0$, $m^*_{2d} = 0.11m_0$ and $\Delta = 40$ meV, where m_0 is the electron mass. All effective masses are considered constant in the entire temperature interval. Further input parameters are taken from the experimental reflectance spectra $R_{\perp c}$, where data at several temperatures are shown in Fig. 1, and measurements of electrical conductivity $\sigma_{\perp c}$, Hall coefficient $R_{H\perp c}$, Seebeck coefficient $S_{\perp c}$, and magnetoresistance coefficient $H_{0\perp c}$, are all shown in Fig. 2. Values of the transport data at selected temperatures are presented in Table 1.

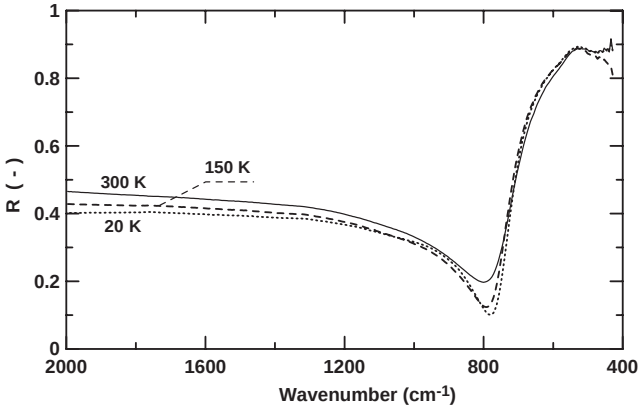

Fig. 1. Measured reflectivity spectra $R_{\perp c}$ of single crystal Bi_2Se_3 at 300, 150 and 20 K.

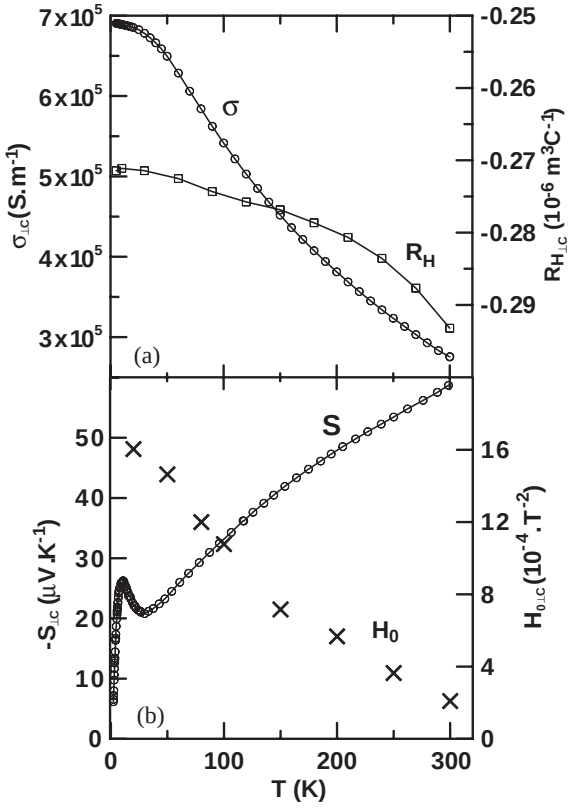

Fig. 2. (a) Temperature dependence of the electrical conductivity ($\sigma_{\perp c}$) and Hall coefficient ($R_{H\perp c}$) and (b) temperature dependence of the thermopower (S) and weak field magnetoresistance coefficient ($H_{0\perp c}$) for single crystal Bi_2Se_3, whose values at 20, 50, 80, 100, 150, 200, 250 and 300 K were used as input data in the presented model.

Table 1
Experimental data on Bi_2Se_3 single crystal

T (K)	$n/m^*_\perp$ ($10^{26}\,m^{-3}$)	$\sigma_{\perp c}$ ($S\,m^{-1}$)	$S_{\perp c}$ ($10^{-6}\,V\,K^{-1}$)	$R_{H\perp c}$ ($10^{-7}\,m^3\,C^{-1}$)	$H_{0\perp c}$ ($10^{-4}\,T^{-2}$)
300	1.93	275,500	−59.0	−2.93	2.09
250	1.88	323,500	−53.5	−2.85	3.64
200	1.79	381,000	−48.0	−2.80	5.67
150	1.74	452,000	−41.0	−2.78	7.16
100	1.67	541,500	−33.0	−2.75	10.8
80	1.66	584,000	−30.0	−2.74	12.0
50	1.62	650,000	−25.5	−2.72	14.6

4.1. Solving the model

As is virtually always the case in the analysis of transport measurements, the theoretical description requires more parameters than the experiment can provide. Consequently, to make the problem tractable, one is forced to make judicious decisions regarding the essential features of the transport including sensible approximations. In the following, we describe how we approach the problem.

First, values of the ratio $n/m^*_{\perp c}$ obtained from fitting the reflectance spectra $R_{\perp c}$ (20–300 K) were used to determine concentrations of both types of carriers n_1 and n_2 and the reduced Fermi level η^* from Eqs. (5)–(8). The obtained values are presented in Table 2. We note that the determination of η^*, n_1, and n_2 does not depend on any particular scattering mechanism. We used these values, in turn, to analyze the galvanomagnetic and thermal transport properties assuming that the charge carriers are subjected to mixed scattering described in Eq. (11).

Before proceeding further, we need to consider the appropriateness of the mixed scattering picture in the context of Bi_2Se_3. The temperature dependence of the measured Hall mobility $R_H\sigma$, shown in Fig. 3, hints at the presence of neutral impurity scattering at low temperatures and near room temperature the slope is close to value $-1/2$, which could correspond to polar-optical scattering. One might consider these two mechanisms as acceptable due to the existence of partially ionic bonding in Bi_2Se_3 crystals, as follows for instance from, the band structure calculations of Mishra [8]. However, we note that isostructural Sb_2Te_3 with high doping levels exhibits a very similar temperature dependence of the Hall mobility [18] and there is no reason to assume optical-polar scattering for this material due to the primarily covalent character of its bonds. We think that a more physically realistic model for this behavior, one employed successfully in a study of Bi_2Se_3 crystals similar to ours [19], is based on the scattering from both acoustic phonons and ionized impurities.

There is supporting evidence for this position: temperature dependence of Hall mobility of low concentration n-type Bi_2Se_3 ($n \sim 10^{16} - 10^{17}\,cm^{-3}$), presented in the inset of Fig. 3, shows [20] a slope very close to $T^{-3/2}$ dependence (acoustic phonon scattering) at temperatures above 40 K, while at low temperatures the electrons appear to scatter on ionized impurities as evidenced by the positive slope of the curve. Ionized impurities in Bi_2Se_3 are believed to be due positively charged selenium vacancies [21], which act as donors. The large carrier density in our crystal gives rise to a degenerate carrier system (see Table 2). Therefore, as opposed to the $T^{3/2}$ mobility temperature dependence characteristic of ionized impurity scattering in a non-degenerate semiconductor, we observe a metal-like, temperature independent mobility at low temperatures. This tendency toward a temperature independent mobility is even apparent in the data on the low carrier concentration Bi_2Se_3 single crystal of Kohler (see inset to Fig. 3) below 10 K. In fact, the same behavior of mobility in Si (e.g., Ref. [22]) and Ge (e.g., Ref. [23]) was understood by considering the same mixed scattering mechanism taking into consideration carrier degeneracy. We thus proceed with an assumption that the transport properties are dominated by both acoustic phonon and ionized impurity scattering whereby the degenerate carrier transport weakens the temperature dependence of the mobility relative to what one expects from an intrinsic semiconductor situation.

Assuming acoustic scattering prevails at higher temperatures (i.e., $a_i < 1$), the values of the coefficients A_i (Eqs. (16a) and (16b)) are very close to unity, and in further calculations are taken as such. Evaluation of the electron mobilities μ_i (using Eqs. (9) and (15)) is only possible provided one or both of the structural factors γ_i differ from unity. In particular, no satisfactory solution for the mobilities is found for other combinations of scattering mechanisms (i.e., different values of A_i) if we insist that $\gamma_1 = \gamma_2 = 1$. It is well established that the LCB in Bi_2Se_3 is described by a single-valley model [24] and thus $\gamma_1 = 1$. Consequently, the structural factor of the UCB must differ from unity, which implies that the UCB has a multi-valley character as suggested in Ref. [7]. To estimate the value of γ_2 we measured the magnetoresistance coefficient $H_{0\perp c}$ (Eq. (18)). Thus,

Table 2
Some values obtained from the model

T (K)	η^*	n_1 (10^{24} m^{-3})	n_2 (10^{24} m^{-3})	n_1/n_2	μ_1 (m^{2}V^{-1}s^{-1})	μ_2 (m^{2}V^{-1}s^{-1})	τ_1 (10^{-14} s)	τ_2 (10^{-14} s)	σ_1 (S m^{-1})	σ_2 (S m^{-1})	a	τ_{1ac0} (10^{-14} s)	τ_{2ac0} (10^{-14} s)	γ_2
300	5.69	11.50	6.25	1.84	0.092	0.106	5.5	4.5	169600	105900	0.82	14.0	10.3	0.56
250	6.79	11.25	6.04	1.86	0.108	0.134	6.4	5.7	194000	129500	1.50	18.1	14.5	0.52
200	8.33	10.80	5.71	1.90	0.127	0.176	7.6	7.5	220500	160500	2.50	24.4	22.3	0.45
150	11.0	10.60	5.50	1.93	0.149	0.226	8.9	9.6	252500	199500	4.40	34.6	36.1	0.42
100	16.2	10.20	5.23	1.96	0.179	0.296	10.7	12.6	293500	248000	8.90	56.3	68.6	0.39
80	20.2	10.20	5.18	1.97	0.192	0.326	11.5	13.9	313000	271000	14.0	76.5	102.0	0.38
50	31.8	9.94	5.02	1.98	0.213	0.386	12.7	16.5	340000	310000	31.5	142.0	230.0	0.36

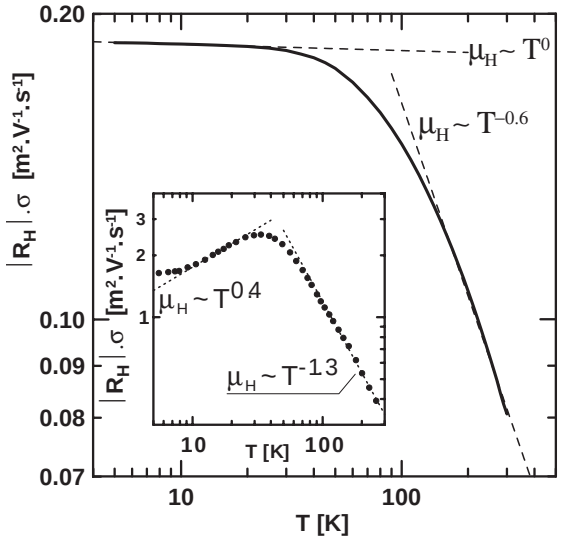

Fig. 3. Measured temperature dependence of the Hall mobility ($R_{H\perp c} \cdot \sigma_{\perp c}$) of single crystal Bi_2Se_3. The inset is data from Ref. [19] on a single crystal of Bi_2Se_3 with much lower carrier concentration (5×10^{17} cm^{-3}).

there are three unknown parameters (μ_1, μ_2, γ_2) in Eqs. (9), (15) and (18).

The above-mentioned system of three non-linear equations leads to four solutions. Two of them are extreme in the sense that one of the calculated mobilities (either μ_1 or μ_2) exceeds the other one by three orders of magnitude. In our opinion this is unlikely and we do not consider this solution any further. From the remaining two solutions we exclude the one which, upon further calculations, fails to fit the measured Seebeck coefficient and yields substantially worse values of the Nernst–Ettinghausen effect in comparison with the observed or published values (unlike the used solution—see below). The results of the fourth solution are presented in Table 2 and in their graphical form are displayed in Figs. 4 and 5, where temperature dependences of the mobility of both carriers (μ_1 and μ_2) and the respective conductivities (σ_1 and σ_2) are given. The solution gives values of the γ_2 factor in the range 0.36–0.56. This range of possible solutions seems quite reasonable. The γ-factors for the isostructural n-Bi_2Te_3 fall in the same range (0.326 [25], 0.398 [26], and 0.4–0.6 [27]).

To determine the respective partial Seebeck coefficients of the two carriers we need to know four parameters a_i and τ_{i0ac} ($i = 1, 2$) from three available Eqs. (12), (13) and (19), in which two-parametric integrals of the form of Eq. (14) are used. The number of parameters can be reduced from four to three by choosing a particular relationship between a_1 and a_2. We decided to use the same value of the ratio of energy independent relaxation times $a^2 = \tau_{ac0}/\tau_{ii0}$ ($a_1 = a_2$). With this simplification we had three variables ($a, \tau_{1ac0}, \tau_{2ac0}$) to satisfy three Eqs. (12), (13) and (19).

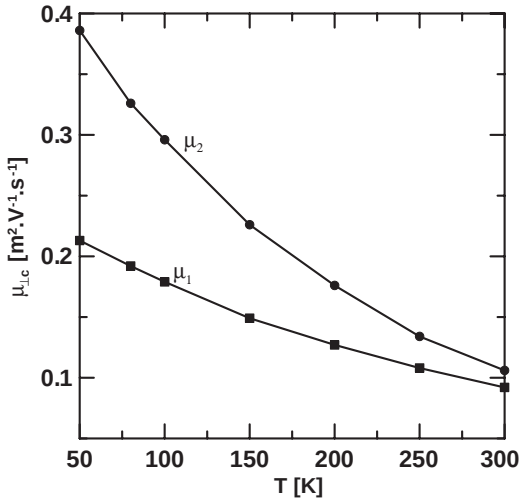

Fig. 4. Calculated mobilities of both types of carriers obtained from the model.

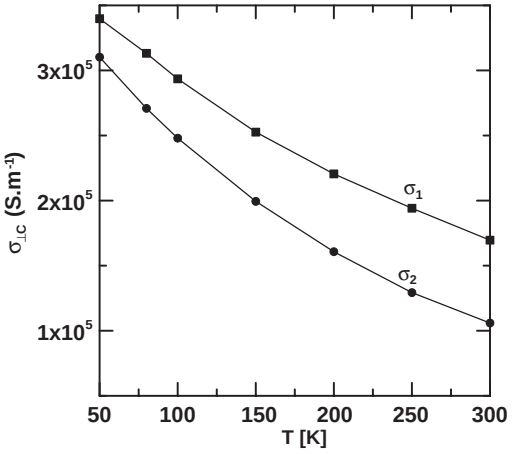

Fig. 5. Calculated partial electrical conductivities of both types of carriers obtained from the model.

After determining these parameters, we were able to calculate the Seebeck coefficients S_1 and S_2 corresponding to the individual carriers. We note that the approximation $a_1 = a_2$ should be considered as a limiting solution. The correct solution lies in the domain $a_1 > a_2$ due to the fact that faster carriers are less influenced by electrostatic forces, i.e., scattering on ionized impurities is less important compared to the case of slower carriers. Here we rely on the findings of Ref. [12] that gives a smaller effective mass to the UCB carriers. To determine the other limit we took an extreme case $a_2 \to 0$ ($a_2 = 0.1$ in our case) and calculated the corresponding value of a_1. Constrained by these limits, we calculated the limiting values of S_1 and S_2 down to temperatures of 50 K. The calculated values of two partial Seebeck coefficients at the two extremes of the a-parameters are presented in Fig. 6. The correct solution for S_1 and S_2 lies between these two limits.

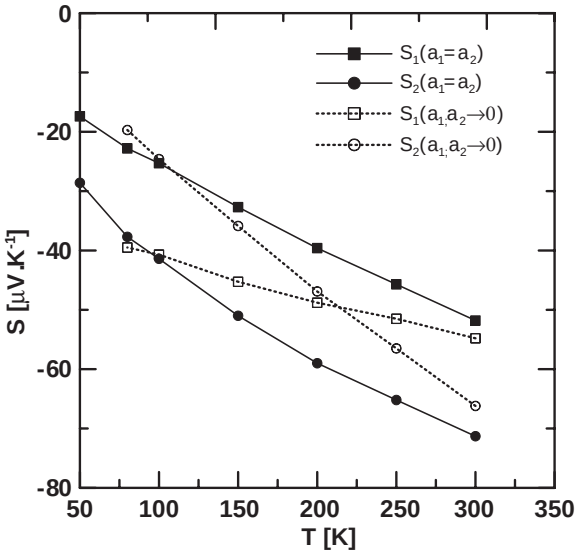

Fig. 6. Solutions of the Seebeck coefficients S_1 and S_2 for case $a_1 = a_2$ (solid lines) and for the case a_1; $a_2 \to 0$ (dashed lines).

Measurements of Nernst–Ettingshausen coefficient Q of our Bi_2Se_3 crystal can help further elucidate the relationship between a_1 and a_2. We were able to measure the value of the coefficient only at 80 K, since at lower temperatures the signal was too small to be determined. We obtained Q (80 K) $= -0.54 \pm 0.08\,\mu V\,T^{-1}\,K^{-1}$. The calculated value under the assumption $a_1 = a_2$ is Q (80 K) $= -0.75\,\mu V\,T^{-1}\,K^{-1}$. In fact, it follows from the analysis that in order to conform to such low Q-values the two a-parameters must be comparable. We have also calculated the value of Q at 300 K ($+0.35\,\mu V\,T^{-1}\,K^{-1}$) and compared it with the published experimental value $+0.6 \pm 0.1\,\mu V\,T^{-1}\,K^{-1}$ [28]. This measurement was made on a crystal with carrier density comparable to our single crystal as judged from the position of the minimum in the reflectivity data. Again, a good agreement between the two values implies that the assumption of $a_1 \approx a_2$ is a reasonable one.

4.2. The calculation of the electronic part of thermal conductivity and evaluation of the lattice thermal conductivity

With the obtained a-parameters we then proceeded to determine contributions of both types of electrons to the total electronic thermal conductivity according to Eqs. (22) and (23). The respective Lorenz numbers for both carriers are presented in Table 3. By calculating the Lorenz numbers L_1 and L_2 for representative values across the entire domain of the a-parameters (i.e., for cases from ($a_1 \to 0$; a_2) to (a_1; $a_2 \to 0$)) we found that L_1 and L_2 are only very weakly dependent on the actual value of the a-parameters (for a given value of η^*). Thus,

Table 3
Results of the calculation of the electronic part of the thermal conductivity

T (K)	L_1 (V^2K^{-2})	L_2 (V^2K^{-2})	κ_{e1} ($W m^{-1} K^{-1}$)	κ_{e2} ($W m^{-1} K^{-1}$)	$\kappa_{etot}(\kappa_{e1}+\kappa_{e2})$ ($W m^{-1} K^{-1}$)	κ_{exp} ($W m^{-1} K^{-1}$)	$\kappa_L(\kappa_{exp}-\kappa_{etot})$ ($W m^{-1} K^{-1}$)
300	2.19e−08	2.05e−08	1.12	0.65	1.77	3.10	1.33
250	2.23e−08	2.09e−08	1.08	0.68	1.76	3.36	1.60
200	2.27e−08	2.15e−08	1.00	0.69	1.69	3.72	2.03
150	2.32e−08	2.22e−08	0.88	0.66	1.54	4.25	2.70
100	2.38e−08	2.32e−08	0.67	0.60	1.27	5.37	4.10
80	2.40e−08	2.36e−08	0.60	0.51	1.11	6.52	5.41
50	2.42e−08	2.41e−08	0.41	0.37	0.78	9.74	8.96

we maintained the $a_1 = a_2$ approximation in the determination of L_1 and L_2.

Subtracting the total electronic thermal conductivity from the measured thermal conductivity one obtains the phonon (or lattice) part of the thermal conductivity, $\kappa_{L\perp c} = \kappa_{\perp c} - \kappa_{e\perp c}$. The total $\kappa_{\perp c}$ as well as the electronic $\kappa_{e\perp c}$ and phonon $\kappa_{L\perp c}$ thermal conductivities are shown in Fig. 7. The temperature dependence of lattice thermal conductivity is normally treated within the Debye approximation. We performed a theoretical fit of $\kappa_{L\perp c}$ for Bi_2Se_3 using the following expression [29]:

$$\kappa_L(T) = \frac{k_B}{2\pi^2 v}\left(\frac{k_B T}{\hbar}\right)^3 \int_0^{\theta_m/T} \tau_c \frac{y^4 e^y}{(e^y-1)^2}\,dy, \qquad (24)$$

where ω is the phonon frequency, k_B is the Boltzmann constant, $\hbar$ is the reduced Planck constant, y stands for the dimensionless parameter $y = \hbar\omega/k_B T$, θ_m is a cuttoff frequency related to the Debye temperature, v is the velocity of sound, and τ_c is the combined phonon scattering relaxation time. This can be written as

$$\tau_c^{-1} = \frac{v}{d} + A\omega^4 + B\omega^2 T \exp\left(-\frac{\theta_D}{CT}\right), \qquad (25)$$

where d is the crystal size and A, B and C are independent of temperature. The terms in Eq. (25) represent boundary scattering, point-defect (Rayleigh) scattering, and phonon–phonon scattering, respectively. The exponential term is an empirical expression and C is often found to be near 3. For θ_D, we use the data of Ure et al. who determined the temperature dependent Debye temperature of Bi_2Se_3 from specific heat measurements [30]. According to Klemens [31], $\theta_m = \theta_D/n^{1/3}$ for crystals made up of molecular groups of n atoms ($n = 5$ for Bi_2Se_3). The smallest dimension of the single crystal (2.5 mm) was used for d and the prefactors A, B and C were fitting parameters. The inset to Fig. 7 displays the lattice thermal conductivity data (open circles) and theoretical fit (solid line) to Eqs. (24) and (25). Fitted values for A, B and C are given in the figure caption.

It is interesting to compare the lattice thermal conductivity of Bi_2Se_3 to that of the isostructural Sb_2Te_3. In the case of Sb_2Te_3 [32], the data could not be fitted below the peak unless electron–phonon

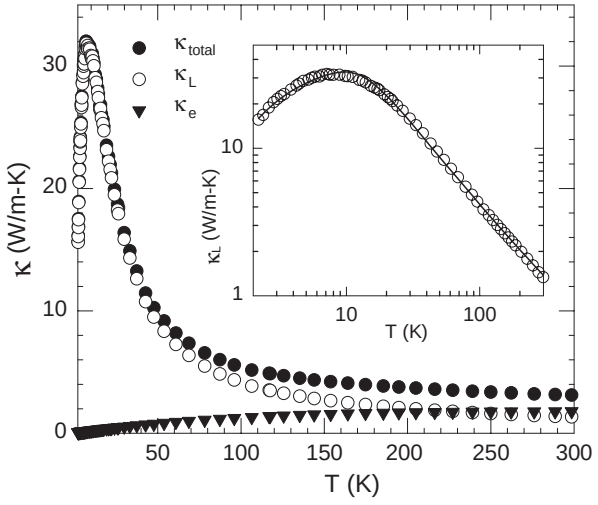

Fig. 7. Temperature dependence of the total thermal conductivity ($\kappa_{\perp c}$) for single crystal Bi_2Se_3 and its electronic ($\kappa_{e\perp c}$) and lattice part ($\kappa_{L\perp c}$) obtained from the model. The inset shows a comparison of κ_L to Debye theory. The solid line is a fit to Eqs. (24) and (25) with $A = 9.42\times10^{-42}\,s^3$, $B = 7.78\times10^{-18}\,s\,K^{-1}$, and $C = 2.8$.

interactions were taken into account using a term in the combined phonon scattering time having the form $D\omega$. Adding a term of this form does not improve the fit for Bi_2Se_3, which implies a weaker interaction between *electrons* and phonons in Bi_2Se_3 than that between *holes* and phonons in the p-type Sb_2Te_3. The phonon–phonon scattering prefactor term B arising from the fits is very close for both materials. On the other hand, A, which is related to the nature and concentration of point defects, is nearly two orders of magnitude larger for Bi_2Se_3 than for Sb_2Te_3. This can be explained by considering that the most prevalent point defects in Bi_2Se_3 are positively charged selenium vacancies. Mass fluctuation scattering in this case is much stronger than in Sb_2Te_3, where the dominant defects are antisite defects with less drastic mass difference and elastic strain than for a vacancy. Therefore, one can expect the point defect parameter A to be much larger for Bi_2Se_3 and these results lend support to the notion that a high concentration of selenium vacancies are present.

5. Conclusions

Electrical and thermal transport properties of a single crystal of Bi_2Se_3 were investigated over a wide temperature range. In order to address the current discrepancy in the literature regarding the presence of both an upper as well as a LCB, we explored a fit of our data to a two-band model using as input the recently reported findings of a band splitting of 40 meV and the respective conduction band effective masses. The model fits our data very well and the results indicate that, unlike the single-valley Γ-point band, the UCB must be described as having a many-valley character. One possible explanation for the fact that some of the band structure calculations predict that this UCB lies much higher in energy than experimental data has shown is that the calculations consider strictly the perfect lattice, whereas in reality the material has a large concentration of selenium vacancies which could alter the relative positions of the band edges.

We were able to determine the contributions of each band to the overall transport behavior of the crystal. In our analysis we assume that the carriers scatter on two distinct entities: acoustic phonons and ionized impurities. Somewhat surprisingly, the ionized impurity scattering influences the transport behavior even at temperatures approaching 300 K. The most likely reason for this strong ionized impurity scattering is the presence of a large number of charged selenium vacancies that seems to be a ubiquitous feature of Bi_2Se_3 crystals. These vacancies act as donors and are responsible for the high carrier degeneracy and weak temperature dependence of the mobility relative to what is expected from non-degenerate carrier statistics. The ratio of the strength of acoustic to impurity scattering is comparable for both types of carriers.

Having ascertained the contribution of each band to the electrical conductivity, we determined the respective electronic parts of the thermal conductivity. Subtracting the total electronic thermal conductivity from the measured thermal conductivity, we obtained the thermal conductivity due to lattice phonons. The temperature dependence of the lattice thermal conductivity could be nicely modeled with the Debye approach in the relaxation time approximation.

Acknowledgments

The authors acknowledge the support of NSF International Grant number 0201114 and of Key Projects of Academy of Sciences of the Czech Republic KSK2050602 and K1010104.

References

[1] D.M. Rowe, in: D.M. Rowe (Ed.), CRC Handbook of Thermoelectrics, CRC Press, Boca Raton, FL, 1995, p. 90.
[2] H.J. Goldsmid, Thermoelectric Refrigeration, Pion Ltd., London, 1986.
[3] K.J. Hashimoto, Phys. Soc. Jpn. 16 (1970) 1961.
[4] H. Koehler, G. Landwehr, Phys. Stat. Sol. B 45 (1971) K109.
[5] H. Koehler, C.R. Becker, Phys. Stat. Sol. B 61 (1974) 533.
[6] H. Koehler, Phys. Stat. Sol. B 62 (1974) 57.
[7] E.V. Oleshko, V.N. Korolyshin, Sov. Phys.—Semicond. 19 (1985) 1130.
[8] S.K. Mishra, S. Satpathy, O. Jepsen, J. Phys.: Condens. Matter 9 (1997) 461.
[9] P. Larson, V.A. Greanya, W.C. Tonjes, R. Liu, S.D. Mahanti, C.G. Olson, Phys. Rev. B 65 (2002) 85108.
[10] H. Koehler, E. Wuechner, Phys. Stat. Sol. B 67 (1975) 665.
[11] H. Koehler, H. Fischer, Phys. Stat. Sol. B 69 (1975) 349.
[12] M. Stordeur, Dissertation B, Martin-Luther-Universitaet, Halle-Wittenberg, 1985, p. 139.
[13] V.A. Kulbachinskii, N. Miura, H. Hakagawa, H. Arimoto, T. Ikaida, P. Lostak, C. Drasar, Phys. Rev. B 59 (1999) 15733.
[14] J. Navrátil, T. Plecháček, J. Horák, S. Karamazov, P. Lošťák, J.S. Dyck, W. Chen, C. Uher, J. Solid State Chem. 160 (2001) 474.
[15] V.I. Fistul, Heavily Doped Semiconductors, Plenum, New York, 1969.
[16] G.M. Korn, R. Braunstein, Phys. Stat. Sol. B 50 (1972) 77.
[17] B.M. Askerov, Electron Transport Phenomena in Semiconductors, World Scientific Publishing Company Inc., 1994.
[18] J.S. Dyck, P. Hájek, P. Lošťák, C. Uher, Phys. Rev. B 65 (2002) 115212.
[19] M. Stordeur, K.K. Ketavong, A. Priemuth, H. Sobota, V. Riede, Phys. Stat. Sol. B 169 (1992) 505.
[20] H. Koehler, A. Fabricius, Phys. Stat. Sol. B 71 (1975) 487.
[21] J. Horák, Z. Starý, P. Lošťák, J. Pancíř, J. Phys. Chem. Solids 51 (1990) 1353.
[22] V.I. Fistul, M.I. Iglitsyn, E.M. Omelyanovskii, Sov. Phys.—Solid State 4 (1962) 784.
[23] E.M. Omelyanovskii, V.I. Fistul, M.G. Milvidskii, Sov. Phys.—Solid State 5 (1963) 676.
[24] H. Koehler, Phys. Stat. Sol. B 58 (1973) 91.
[25] J.R. Drabble, R.D. Groves, R. Wolfe, Proc. Phys. Soc. 71 (1958) 430.
[26] R.B. Mallison, J.R. Rayne, R.W. Ure, Phys. Rev. 175 (1968) 1049.
[27] L.P. Caywood, G.R. Miller, Phys. Rev. B 2 (1970) 3209.
[28] M. Matyáš, J. Horák, L. Tichý, Physics of Narrow Gap Semiconductors, PWN-Polish Scientific Publishers, Warszawa, 1978.
[29] J. Callaway, Phys. Rev. 113 (1959) 1046.
[30] G.E. Shoemaker, J.A. Rayne, R.W. Ure, Phys. Rev. 185 (1969) 1046.
[31] M. Roufosse, P.G. Klemens, Phys. Rev. B 7 (1973) 5379.
[32] J.S. Dyck, W. Chen, C. Uher, C. Drašar, P. Lošťák, Phys. Rev. B 66 (2002) 125206.